JGR

RESEARCH ARTICLE

Key Points:
- Study crustal field, solar cycle, and seasons on Mars' upper atmosphere ion escape
- To understand the long-term evolution of Mars atmosphere over its history
- To support MAVEN spacecraft mission data analysis (2014–2016)

Correspondence to:
C. Dong,
dcfy@umich.edu

Solar wind interaction with the Martian upper atmosphere: Crustal field orientation, solar cycle, and seasonal variations

Chuanfei Dong[1], Stephen W. Bougher[1], Yingjuan Ma[2], Gabor Toth[1], Yuni Lee[1], Andrew F. Nagy[1], Valeriy Tenishev[1], Dave J. Pawlowski[3], Michael R. Combi[1], and Dalal Najib[4]

[1]Department of Atmospheric, Oceanic and Space Sciences, University of Michigan, Ann Arbor, Michigan, USA, [2]Department of Earth and Space Sciences, University of California, Los Angeles, California, USA, [3]Department of Physics and Astronomy, Eastern Michigan University, Ypsilanti, Michigan, USA, [4]National Academy of Sciences, Washington, District of Columbia, USA

Abstract A comprehensive study of the solar wind interaction with the Martian upper atmosphere is presented. Three global models: the 3-D Mars multifluid Block Adaptive Tree Solar-wind Roe Upwind Scheme MHD code (MF-MHD), the 3-D Mars Global Ionosphere Thermosphere Model (M-GITM), and the Mars exosphere Monte Carlo model Adaptive Mesh Particle Simulator (M-AMPS) were used in this study. These models are one-way coupled; i.e., the MF-MHD model uses the 3-D neutral inputs from M-GITM and the 3-D hot oxygen corona distribution from M-AMPS. By adopting this one-way coupling approach, the Martian upper atmosphere ion escape rates are investigated in detail with the combined variations of crustal field orientation, solar cycle, and Martian seasonal conditions. The calculated ion escape rates are compared with Mars Express observational data and show reasonable agreement. The variations in solar cycles and seasons can affect the ion loss by a factor of ~3.3 and ~1.3, respectively. The crustal magnetic field has a shielding effect to protect Mars from solar wind interaction, and this effect is the strongest for perihelion conditions, with the crustal field facing the Sun. Furthermore, the fraction of cold escaping heavy ionospheric molecular ions [(O_2^+ and/or CO_2^+)/Total] are inversely proportional to the fraction of the escaping (ionospheric and corona) atomic ion [O^+/Total], whereas O_2^+ and CO_2^+ ion escape fractions show a positive linear correlation since both ion species are ionospheric ions that follow the same escaping path.

1. Introduction

The Sun has a powerful influence on planetary atmospheres. Annual changes in temperature on a planet are caused by a combination of two factors: axial tilt and variations in the distance from the Sun. On Earth, the axial tilt determines nearly all of the annual variations, because Earth's orbit is nearly circular. Mars, however, has the highest orbital eccentricity of any planet except Mercury; the distance from the Sun to Mars varies approximately from 1.38 AU to 1.66 AU over a Martian year. This large variation, combined with an axial tilt (25.19°) slightly greater than Earth's (23.4°), gives rise to seasonal variations far greater than those we experience even in the coldest areas on our own planet [*de Pater and Lissauer*, 2010]. Furthermore, Mars has no global intrinsic dipole magnetic field; instead, it has a crustal magnetic field, which was first discovered by the Mars Global Surveyor (MGS) spacecraft [*Acuña et al.*, 1999]. The crustal fields, B_c, are distributed about the surface of the planet in a very inhomogeneous manner, which plays an important role in the process of solar wind planet interaction. The strongest crustal sources are located at latitudes poleward of 30°S and at longitudes between 120° and 240°E [*Acuña et al.*, 1999].

Atmospheric dynamics and chemistry are greatly affected by temperature, suggesting that the entire Mars atmosphere is an integrated system that must be treated as a whole from the ground to the exobase (~0 to 250 km) [*Bougher et al.*, 2015]. In fact, strong coupling processes are known to link the Mars lower to upper atmospheres [e.g., *Bougher et al.*, 2014]. These processes are crucial to be quantified in order to reliably predict upper atmosphere densities, temperatures, winds, planetary waves (e.g., tides and gravity waves) over various timescales (e.g., solar cycle, seasonal, and diurnal). Three-dimensional "whole atmosphere" models are ultimately required to capture these coupling processes (e.g., thermal, chemical, and dynamical) throughout the entire Mars atmosphere. The 3-D Mars Global Ionosphere Thermosphere Model (M-GITM)

[*Bougher et al.*, 2015] is such a model that can generate a relatively realistic Martian atmosphere with detailed structures that incorporates the effects of solar cycle and seasonal variations. Cold neutral atoms and molecules in this paper refer to the thermal particles, and hot oxygen refers to those from dissociative recombination of O_2^+. Basically, the hot oxygen has a thermal speed larger than the local background thermal speed (calculated based on M-GITM thermospheric profile [*Bougher et al.*, 2015]), indicating the scale height of hot oxygen is larger than that of the cold oxygen [e.g., *Ma et al.*, 2004, Figures 1 and 2]. However, the hot oxygen can be converted to the thermal oxygen via collisions with other background cold neutral species before it escapes to interplanetary space [*Lee et al.*, 2013]. It is noteworthy that when we mention the cold heavy ionospheric molecular/atomic ions, it refers to those ionized from the cold molecular/atomic neutrals. However, these ions can be accelerated to relatively high energy during their escape.

The weak gravity of Mars allows an extended corona of hot species to be present [*Valeille et al.*, 2009]. Among all the chemical reactions, dissociative recombination of O_2^+ ($O_2^+ + e \longrightarrow O + O + \text{energy}$) is the most important one, which is responsible for most of the production of dayside exospheric hot atomic oxygen. Besides, the sputtering caused by pickup ion (e.g., O^+) collisions with the Martian atmospheric neutral species is also an important source for the hot corona [*Johnson and Luhmann*, 1998]. There are hot hydrogen and carbon coronae as well [*Lee et al.*, 2014a].

The cold exospheric oxygen component [e.g., see *Ma et al.*, 2004, Figures 1 and 2] also plays an important role in the solar wind interaction with the Martian upper atmosphere, especially below 600 km [*Feldman et al.*, 2011]. In order to reproduce a realistic asymmetric corona of hot species from observations, a 3-D global kinetic exosphere model is required, especially above the exobase (Knudsen number, $K_n \approx 1$) where the fluid assumption usually fails [*Lee et al.*, 2013]. One such model is the Mars exosphere Monte Carlo model Adaptive Mesh Particle Simulator (M-AMPS) [*Tenishev and Combi*, 2008; *Lee et al.*, 2013, 2014a, 2014b], which can generate a 3-D hot (e.g., oxygen and carbon) corona with detailed asymmetric structure. In order to capture these 3-D asymmetries, 3-D thermosphere/ionosphere inputs from a validated ground-to-exobase atmospheric model (e.g., M-GITM) are essential (see Figure 1 for more detail).

Over the last 30 years, a series of spacecraft with plasma instrumentation have been sent to Mars (e.g., Phobos 2, Mars Global Surveyor (MGS), and Mars Express (MEX) missions). The recent NASA Mars Atmosphere and Volatile EvolutioN (MAVEN) mission was launched on 18 November 2013 and successfully entered an orbit around Mars on 21 September 2014. MAVEN will explore the Mars upper atmosphere, ionosphere, and interactions with the solar EUV radiation and solar wind environment and determine the role that loss of volatiles to space has played through time. Recently, the study of the solar wind interaction with Mars upper atmosphere/ionosphere has received a great deal of attention, especially the investigation of ion escape rates due to its potential impact on the long-term evolution of Mars atmosphere (e.g., loss of water) over its history. A number of papers reporting on the measurement of ion escape rates by the ASPERA-3 instrument on the Mars Express spacecraft have also been published [e.g., *Barabash et al.*, 2007; *Lundin et al.*, 2008, 2009, 2013; *Nilsson et al.*, 2011]. In *Lundin et al.* [2013], they reported that the average heavy ion escape rate is increased by a factor of ~10, from ~1 ×10^{24} s^{-1} (solar minimum) to ~1 ×10^{25} s^{-1} (solar maximum). On the other hand, both *Verigin et al.* [1991] (by Phobos-2 observations) and *Nilsson et al.* [2011] suggested that high solar activity leads to ~2.5 times higher ion escape rate than the low solar activity result.

It is difficult to accurately estimate global ion escape rates from spacecraft data due to the complex geometry of loss regions around Mars. Thus, the use of global simulations is necessary. Various plasma models based on different assumptions, i.e., test particle model [*Fang et al.*, 2010; *Curry et al.*, 2013, 2014, 2015], multispecies MHD model [*Ma et al.*, 2004; *Ma and Nagy*, 2007; *Ma et al.*, 2014], multifluid MHD model [*Harnett and Winglee*, 2006; *Najib et al.*, 2011; *Riousset et al.*, 2013, 2014; *Dong et al.*, 2014], and kinetic hybrid model [*Modolo et al.*, 2012; *Brecht and Ledvina*, 2014a] have been used to simulate the solar wind interaction with the Martian upper atmosphere and calculate the associated ion escape rates. An ongoing International Space Studies Institute effort focused upon the global models and measurements of the Martian plasma environment being led by Professor David Brain at the University of Colorado, Boulder, CO [*Brain et al.*, 2010, 2012], allows intercomparison of these multidimensional plasma codes, which will benefit the entire community. However, there have been no systematic studies on the effects of crustal field orientation, solar cycle, and season on the Martian upper atmosphere ion escape by using the variable 3-D cold neutral thermosphere and hot oxygen corona as inputs in a plasma code.
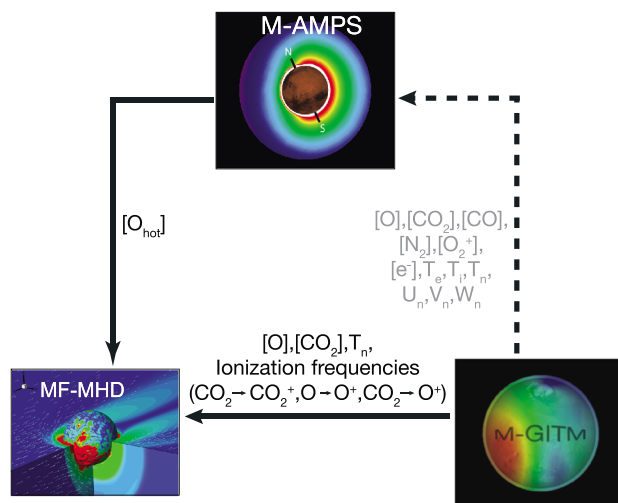
Figure 1. A sketch of a one-way coupling approach between M-GITM, M-AMPS, and the multifluid MHD (MF-MHD) model. The notation T_n denotes neutral atmosphere temperatures, [O], [CO_2], and [O_{hot}] are the neutral O, CO_2, and hot atomic oxygen number densities. Three photoionization processes are included. Here we focus on the one-way coupling indicated by the solid line. For the detailed study of one-way coupling between M-GITM and M-AMPS (dashed line), please refer to *Lee et al.* [2013, 2014a, 2014b].

In the present work, we study the solar wind interaction with the Martian upper atmosphere by using a one-way coupling of three comprehensive 3-D models, i.e., the M-GITM thermosphere-ionosphere model outputs (i.e., neutral atmosphere temperatures T_n, neutral densities n_O, n_{CO_2}, and photoionization frequencies I_O, I_{CO_2}) and the M-AMPS hot atomic oxygen corona densities ($n_{O_{hot}}$) are used as inputs for the Block Adaptive Tree Solar-wind Roe Upwind Scheme (BATS-R-US) Mars multifluid MHD (MF-MHD) model (see Figure 1 for the one-way coupling framework). The MF-MHD code solves separate continuity, momentum, and energy equations for each ion species [*Powell et al.*, 1999; *Glocer et al.*, 2009; *Najib et al.*, 2011; *Tóth et al.*, 2012; *Dong et al.*, 2014]. Please refer to *Lee et al.* [2013, 2014a, 2014b] for the detailed study of one-way coupling between M-GITM and M-AMPS (as indicated by the dashed line in Figure 1); i.e., M-GITM provides thermosphere/ionosphere background as an input into the M-AMPS exosphere model. These calculations are carried out for 22 cases with combinations of different crustal field orientations (four cases without crustal field), solar cycle, and Martian seasonal conditions.

The rest of this paper is organized as follows. In section 2, three models are briefly introduced together with the one-way coupling approach depicted in more detail. In section 3, simulation results are presented and discussed based on the comparisons of 22 selected cases. In the last section, conclusions are summarized.

2. Model Descriptions

In this section, we will briefly introduce the Mars Global Ionosphere Thermosphere Model (M-GITM) [*Bougher et al.*, 2015], the Mars exosphere Monte Carlo model Adaptive Mesh Particle Simulator (M-AMPS) [*Lee et al.*, 2013, 2014a, 2014b], and the 3-D BATS-R-US Mars multifluid MHD (MF-MHD) model [*Najib et al.*, 2011; *Dong et al.*, 2014]. All these models are being used to generate a model library of simulated outputs for the MAVEN mission (2014–2016).

2.1. Mars Global Ionosphere Thermosphere Model

Mars Global Ionosphere Thermosphere Model (M-GITM) [*Bougher et al.*, 2015] is a 3-D whole atmosphere code that captures both the Mars lower atmosphere and its thermosphere-ionosphere. The applied domain of this model is 0–250 km (ground-to-exobase). Lower, middle, and upper atmosphere processes are included, based in part upon formulations used in previous lower atmosphere (NASA Ames Mars General Circulation Model [e.g., *Haberle et al.*, 1999]) and upper atmosphere (NCAR Mars Thermospheric General Circulation Model [e.g., *Bougher et al.*, 2000]) models. The typical horizontal grid resolution of M-GITM is 5° × 5° (latitude-longitude), and the vertical coordinate is $\Delta z = 2.5$ km (~0.25 scale height). This model can calculate the neutral global fields including the temperatures (T_n) and the neutral wind velocities (U_n, V_n, and W_n), where the vertical velocity is calculated explicitly for each species. The major neutral species are O, O_2, CO_2, CO, N_2, and Ar, and the minor neutral species, N(^{4}S), N(^{2}D), NO, He, and H_2, will be included soon. The major ions are CO_2^+, O^+, O_2^+, N_2^+, and NO^+, which are calculated assuming photochemical equilibrium. Subcycling is used for ion-neutral chemistry. Due to the relatively large scale height, hydrogen can only be calculated self-consistently by implementing the two-way coupling between the M-GITM and the M-AMPS models. Therefore, currently M-GITM does not include the calculation of hydrogen. There is no hydrostatic assumption in this model; thus, it can deal with large vertical velocities [*Ridley et al.*, 2006; *Deng et al.*, 2008]. It is noteworthy that the previous Mars Thermospheric General Circulation Model (M-TGCM) is based on the hydrostatic assumption
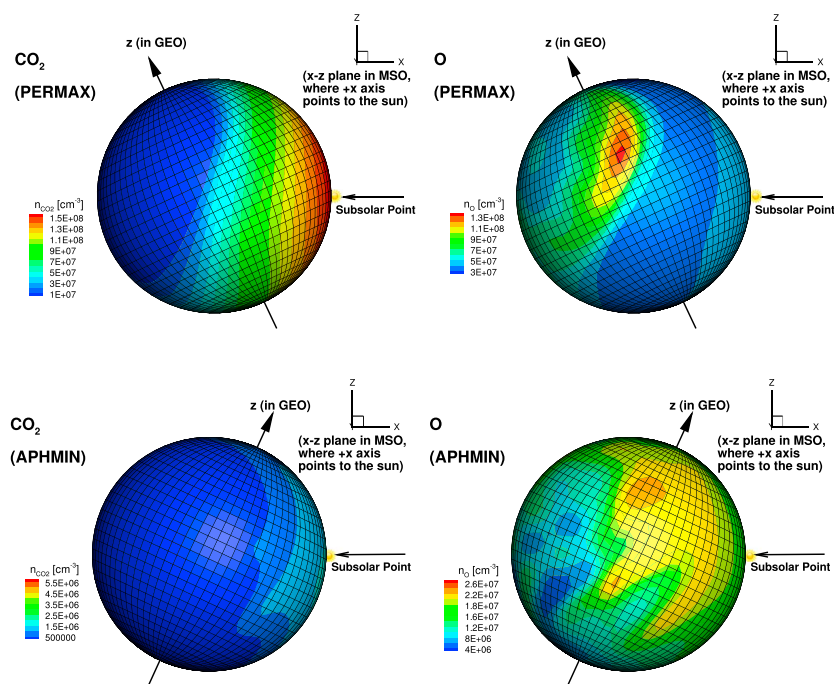
Figure 2. The neutral CO_2 and O number densities shown on a sphere at an altitude of 220 km above the Martian surface from M-GITM for perihelion solar maximum (PERMAX) and aphelion solar minimum (APHMIN) conditions. Two coordinate systems are indicated in each plot: the Geographic (GEO) and the Mars-centered Solar Orbital (MSO) coordinate systems. The spherical contour plots are shown in the *x-z* plane (not a *x-z* cut) of both coordinates. The subsolar point is highlighted in each plot.

[*Bougher et al.*, 2000, 2006] and thus cannot deal with large vertical winds appropriately, especially when experiencing extreme events, such as interplanetary coronal mass ejections (ICMEs) and solar energetic particles (SEPs) heating.

Detailed M-GITM simulations have been conducted over the past few years, spanning various seasonal, solar cycle, and dust conditions [*Bougher et al.*, 2015]. Model validation thus far has focused upon simulations for solar longitude Ls = 90, 180, and 270 for both solar minimum ($F_{10.7}$ = 70) and solar maximum ($F_{10.7}$ = 200) conditions. The solar longitude, Ls, is the Mars-Sun angle, measured from the northern hemisphere spring equinox, where Ls = 0. Specific studies compare M-GITM simulated temperatures and neutral/ion densities against (a) in situ Viking 1 descent measurements for aphelion solar minimum conditions and (b) very limited Mariner 6-7 flyby measurements for perihelion solar maximum conditions (see *Bougher et al.* [2015] for more detail).

Figure 2 illustrates the CO_2 and O densities on a sphere of altitude 220 km for these two extreme conditions. Interestingly, great dayside-nightside asymmetry and detailed local structure are clearly shown in these four density contour plots, demonstrating the importance of adopting 3-D M-GITM neutral outputs. Besides, two coordinate systems are shown in Figure 2: the Geographic (GEO) and the Mars-centered Solar Orbital (MSO) coordinate systems. These plots are shown on a 2-D spherical surface with the rotation axis parallel to both *x-z* plane (in MSO coordinates) and the plane of the paper, where the subsolar point is highlighted in each plot. Clearly, there is an angle of 25.19° between the two *z* axes due to the axial tilt.

2.2. Mars Adaptive Mesh Particle Simulator Model

The University of Michigan Adaptive Mesh Particle Simulator (AMPS) code was first developed to solve the Boltzmann equation of the gas flow in the coma of a comet [*Tenishev and Combi*, 2008]. The AMPS code is developed within the framework of the Direct Simulation Monte Carlo (DSMC) method [*Bird*, 1994], which employs a stochastic solver for both the linear and nonlinear Boltzmann equations. As a standard numerical method today, the DSMC method can represent the collisional dynamics of a finite number of model particles in a rarefied gas flow regime, such as Mars upper atmosphere. Instead of solving the intractable Boltzmann equation, AMPS simulates the ensemble of model particles and captures the physics of the distribution of
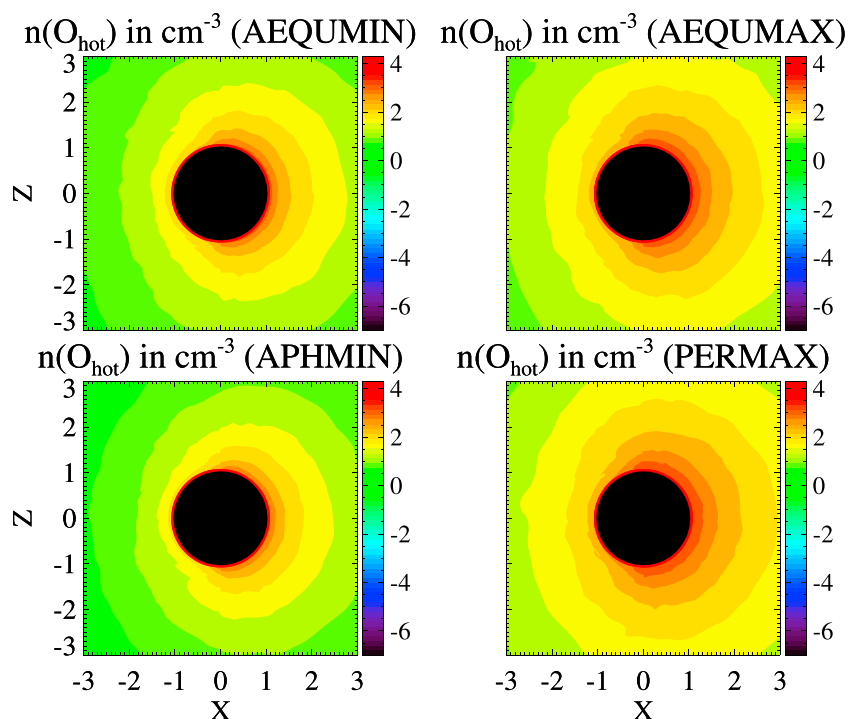
Figure 3. A comparison of the M-AMPS output hot oxygen number density (in cm^{-3}) distribution between (top row) autumnal equinox solar minimum (AEQUMIN, case 7) and maximum (AEQUMAX, case 10) conditions, and (bottom row) aphelion solar minimum (APHMIN, case 1) and perihelion solar maximum (PERMAX, case 16) conditions in the x-z plane in the MSO coordinate system. All the results are based on the subsolar longitude (SSL) = 0. Note the use of a logarithmic scale.

gas species in tenuous upper atmospheres, where the transitions from a local thermodynamic equilibrium (LTE) region to a non-LTE region occur. To model the Martian hot atomic coronae, M-AMPS was run as a test particle Monte Carlo model with a stationary background atmosphere supplied by M-GITM (as indicated by the dashed line in Figure 1), completing the one-way coupling framework [*Lee et al.*, 2013, 2014a, 2014b]. Each hot particle in this coupling framework travels within the influence of the planet's gravitational field and collides with background species from M-GITM before escaping to space or being thermalized in the thermosphere. The nominal cell size is about 60 km at the lower boundary of the computational domain, and the maximum cell size is determined by the designated upper boundary of the domain. M-AMPS includes a data table, which keeps all the information from M-GITM. All the macroparticles in M-AMPS are initialized based on the thermospheric profile in the data table [*Lee et al.*, 2014a, 2014b]. The collision frequencies between different particle species are also evaluated based upon the thermospheric information stored in the data table. The computational domain extends from 100 km above the Martian surface to 5 R_M, where R_M is the radius of Mars (~3396 km).

Recently, *Lee et al.* [2013, 2014a, 2014b] have successfully finished the one-way coupling between M-AMPS and M-GITM (see Figure 1). This coupling approach has been used to calculate both the Martian exosphere hot atomic carbon and oxygen coronae [*Lee et al.*, 2013, 2014a, 2014b]. Figure 3 shows the hot atomic oxygen number density distribution in a logarithmic scale from the 3-D M-AMPS code. Figure 3 (top row) shows the autumnal equinox solar minimum (AEQUMIN, left) and maximum (AEQUMAX, right) conditions, and Figure 3 (bottom row) illustrates aphelion solar minimum (APHMIN, left) and perihelion solar maximum (PERMAX, right) conditions.

By comparing these four cases, the hot atomic oxygen corona is the most extensive and has the highest O$_{hot}$ abundance for the PERMAX conditions, followed by the AEQUMAX case; the hot atomic oxygen corona for the APHMIN conditions is the weakest. Furthermore, all these plots clearly show the asymmetric features of the hot atomic oxygen distribution, indicating that in order to accurately calculate the ion escape rate, it is essential to adopt the 3-D hot oxygen corona in a plasma code.

2.3. BATS-R-US Mars Multifluid MHD Model

The University of Michigan 3-D BATS-R-US multifluid MHD (MF-MHD) model was initially developed for Earth [*Powell et al.*, 1999; *Glocer et al.*, 2009; *Tóth et al.*, 2012] and later it was developed for studies of Mars [*Najib et al.*, 2011; *Dong et al.*, 2014]. The Mars MF-MHD model solves separate continuity, momentum, and energy equations for the four ion fluids H^+, O^+, O_2^+, and CO_2^+. Although the multispecies MHD (MS-MHD) model solves separate ion continuity equations, it only solves one momentum and one energy equations for different ion species [*Ma et al.*, 2004]. Technically speaking, the MF-MHD model is more complete than the MS-MHD code [*Ma et al.*, 2004; *Ma and Nagy*, 2007] because it can better simulate the solar wind planet interaction by considering the dynamics of individual ion species. The MS-MHD model, however, is computationally much cheaper than the MF-MHD model. In order to capture the dynamics of individual ion species, we adopt the MF-MHD model.

Different from the Earth version, the Mars MF-MHD model contains an ionosphere, and thus, the lower boundary (i.e., the surface of a sphere at the lowest altitude in the simulation domain) was extended down to 100 km above the Martian surface. Detailed ionospheric chemistry is included, i.e., charge exchange, photoionization, and electron impact ionization. In order to calculate the latter, the model assumes that the electron temperature is half of the calculated plasma temperature and uses the ionization rates given by *Cravens et al.* [1987]. The same chemical reaction schemes in *Ma et al.* [2004] and *Najib et al.* [2011] are used, but with more realistic collision frequencies between species [*Schunk and Nagy*, 2009]. At the model lower boundary, the densities of O^+, O_2^+, and CO_2^+ satisfy the photochemical equilibrium condition (refer to chapters 8 and 13 (e.g., Figure 13.1) of *Schunk and Nagy* [2009] for detailed ionospheric chemistry), and the velocity **u** is set to satisfy a reflective boundary condition, which leads to approximately zero velocity at the inner boundary, as expected. At the inner boundary, both ions and electrons have roughly the same temperature as the neutrals due to collisions. Therefore, it is a reasonable assumption to set the plasma temperature to be twice the neutral temperature (i.e., $T_{plasma} = T_i + T_e = 2T_n$). The crustal fields are implemented by the 60° harmonic expansion developed by *Arkani-Hamed* [2001], which can well describe the observed fields at Mars [*Acuña et al.*, 1999] and is particularly good at the MGS altitude (∼400 km). A nonuniform, spherical grid structure is used in the model, where the radial resolution varies from 5 km (∼0.5 scale height, i.e., the vertical distance over which the density and pressure fall by a factor of $1/e$ at the lower boundary (∼100 km) to 1000 km at the outer boundary (∼20 R_M). The angular resolution varies from 1.5° to 3.0° (latitude-longitude). The simulation domain is defined by $-24\,R_M \leq X \leq 8\,R_M$; $-16\,R_M \leq Y, Z \leq 16\,R_M$.

Recently, *Dong et al.* [2014] successfully employed a one-way coupling between the MF-MHD model and the 3-D M-TGCM model [*Bougher et al.*, 2000, 2006] along with a 1-D spherically symmetric hot corona model [*Kim et al.*, 1998] to study the effects of the 3-D cold neutral atmosphere on ion escape rates. However, *Dong et al.* [2014] did not investigate the effects of varying inhomogeneous crustal field orientations and seasons on the Martian upper atmosphere ion loss. Moreover, as we described above, the M-TGCM model may not be able to handle the extreme cases (i.e., resulting in large vertical velocities) due to the hydrostatic assumption. M-TGCM is an upper atmosphere model which takes the NASA Ames Mars General Circulation Model outputs as its lower boundary conditions [see *Bougher et al.*, 2008].

The MF-MHD model uses a nonuniform spherical grid in MSO coordinate system, M-GITM uses a uniform spherical grid in GEO coordinate system, and M-AMPS adopts a nonuniform Cartesian grid in GEO coordinate system. In order to one-way couple the MF-MHD model with M-GITM and AMPS, we first need to carry out a coordinate transformation and linear interpolation between different grids. For the hot atomic oxygen, the AMPS output is able to cover the MF-MHD simulation domain from 100 km to 5 R_M. For the M-GITM cold neutral profiles, we use the linear interpolation to cover the MF-MHD domain from 100 km to 220 km. From 220 km to 5 R_M, we assume constant neutral temperatures and photoionization frequencies, based on the M-GITM values since these values are almost constant when approaching 220 km. For the neutral atmosphere densities, however, we use an extrapolation based upon the hydrostatic assumption which assumes the neutral atmosphere densities decrease exponentially with altitude, i.e., $n = n_0 \exp(-dz/H_s)$, where dz is the altitude change and H_s is the scale height (which depends on the gravity, neutral temperature, and neutral species mass). Technically speaking, the hydrostatic assumption may not be accurate enough to describe the cold oxygen component in the Martian exosphere, which should dominate the hot component up to 600 km in altitude [*Feldman et al.*, 2011]. However, the comparison of model results (from the one-way coupling between M-GITM and M-AMPS, Y. Lee et al., Hot oxygen corona at Mars and the photochemical escape of oxygen - Improved description of the thermosphere, ionosphere and exosphere, submitted to *Journal of Geophysical Research:*

Table 1. Input Parameters Used for Different Calculations

Simulation Cases	Subsolar Longitude (SSL)	Solar Cycle Conditions	Seasonal Variations
Case 1	0°W	Solar Minimum	
Case 2	180°W	(APHMIN)	
Case 3	270°W		Aphelion
Case 4	0°W	Solar Maximum	(APH)
Case 5	180°W	(APHMAX)	
Case 6	270°W		
Case 7	0°W	Solar Minimum	
Case 8	180°W	(AEQUMIN)	
Case 9	270°W		Autumnal Equinox
Case 10	0°W	Solar Maximum	(AEQU)
Case 11	180°W	(AEQUMAX)	
Case 12	270°W		
Case 13	0°W	Solar Minimum	
Case 14	180°W	(PERMIN)	
Case 15	270°W		Perihelion
Case 16	0°W	Solar Maximum	(PER)
Case 17	180°W	(PERMAX)	
Case 18	270°W		
Case 19	180°W	APHMIN	Aphelion and Perihelion
Case 20	180°W	APHMAX	comparison with
Case 21	180°W	PERMIN	crustal magnetic field
Case 22	180°W	PERMAX	turned off

Planets, 2015) and ALICE/Rosetta observations of the OI 1304 Å brightness [*Feldman et al.*, 2011] shows good agreement with each other on the transition altitude from cold to hot oxygen (~600 km), indicating that our extrapolation approach is reasonable. It is noteworthy that the cold oxygen component also plays an important role in the solar wind-Mars interaction, especially below 600 km. The cold and hot corona components should be able to be calculated self-consistently in the future by adopting the two-way coupling approach (Figure 1).

3. Simulation Results and Discussion

In this section, we discuss the simulation results by implementing the one-way coupling approach mentioned in section 2; i.e., both the M-GITM and M-AMPS 3-D outputs are used as the inputs for the MF-MHD model (Figure 1). In order to evaluate the effects of different crustal field orientations, plus various solar cycle and seasonal conditions on the Mars upper atmosphere ion loss, we study 18 standard cases plus four cases without crustal fields. The 18 cases combine three crustal field orientations (subsolar longitude, SSL = 0°W, 180°W, 270°W), three Martian seasons (aphelion, autumnal equinox, and perihelion) with solar maximum ($F_{10.7} = 200$) and solar minimum ($F_10.7 = 70$) conditions. Due to the fact that there is no significant difference between vernal equinox and autumnal equinox (the heliospheric distance difference between these two cases is not zero but small), we only study the latter. For all the cases, the solar wind density is set to 4 cm^{-3}, the upstream solar wind plasma temperature is set to 3.5 ×10^5 K, the interplanetary magnetic field (IMF), **B**, is assumed to be a Parker spiral in the *X-Y* plane of MSO coordinate system with an angle of 56°, and the solar wind velocity is 400 km/s. Table 1 summarizes the cases studied in this paper.

The calculated ion escape rates (in ×10^{24} s^{-1}) are summarized in Table 2, and the corresponding histograms are shown in Figure 4. The calculation of ion escape rate is conducted by integrals of the plasma density multiplied by the radial velocity component at the surface of a sphere far from the planet. Given the fact that the calculated ion escape rates do not change to any significant degree once the radius exceeds 4 R_M, we

Table 2. Calculated Ion Escape Rates (in $\times 10^{24}$ s^{-1})

Simulation Cases	O^+	O_2^+	CO_2^+	Total	$(O_2^+ + CO_2^+)/O^+$	CO_2^+/Total (%)
Case 1 (APHMINSSL0)	0.30	1.43	0.13	1.86	5.27	6.87
Case 2 (APHMINSSL180)	0.27	1.65	0.20	2.12	6.75	9.30
Case 3 (APHMINSSL270)	0.32	1.70	0.17	2.18	5.90	7.67
1−3 average (APHMIN)	0.30	1.59	0.16	2.05	5.95	7.99
Case 4 (APHMAXSSL0)	3.08	2.84	0.38	6.29	1.04	5.98
Case 5 (APHMAXSSL180)	2.64	2.38	0.41	5.44	1.06	7.63
Case 6 (APHMAXSSL270)	3.17	2.72	0.44	6.33	1.00	6.92
4−6 average (APHMAX)	2.96	2.64	0.41	6.02	1.03	6.81
1−6 average (APH)	1.63	2.12	0.29	4.03	1.48	7.11
Case 7 (AEQUMINSSL0)	0.41	1.68	0.15	2.24	4.42	6.90
Case 8 (AEQUMINSSL180)	0.31	1.12	0.11	1.53	4.01	6.89
Case 9 (AEQUMINSSL270)	0.44	1.45	0.13	2.02	3.60	6.46
7−9 average (AEQUMIN)	0.39	1.42	0.13	1.93	4.00	6.74
Case 10 (AEQUMAXSSL0)	4.57	2.52	0.26	7.35	0.61	3.49
Case 11 (AEQUMAXSSL180)	3.81	1.80	0.24	5.86	0.54	4.16
Case 12 (AEQUMAXSSL270)	4.99	2.17	0.24	7.40	0.48	3.25
10−12 average (AEQUMAX)	4.46	2.17	0.25	6.87	0.54	3.59
7−12 average (AEQU)	2.42	1.79	0.19	4.40	0.82	4.29
Case 13 (PERMINSSL0)	0.49	1.63	0.13	2.25	3.55	5.67
Case 14 (PERMINSSL180)	0.49	1.51	0.14	2.14	3.34	6.57
Case 15 (PERMINSSL270)	0.71	2.06	0.17	2.94	3.16	5.79
13−15 average (PERMIN)	0.56	1.73	0.15	2.44	3.33	5.98
Case 16 (PERMAXSSL0)	5.07	3.08	0.48	8.63	0.70	5.56
Case 17 (PERMAXSSL180)	4.02	2.40	0.38	6.80	0.69	5.62
Case 18 (PERMAXSSL270)	5.51	3.39	0.53	9.43	0.71	5.64
16−18 average (PERMAX)	4.86	2.96	0.46	8.29	0.70	5.61
13−18 average (PER)	2.71	2.35	0.31	5.37	0.98	5.69
1−3 and 7−9 and 13−15 average (SOLARMIN)	0.42	1.58	0.15	2.14	4.16	6.85
4−6 and 10−12 and 16−18 average (SOLARMAX)	4.10	2.59	0.37	7.06	0.72	5.30
1−18 average (ALL)	2.26	2.08	0.26	4.60	1.04	5.66
Case 19 (APHMINSSL180 [no B_c])	0.46	2.13	0.20	2.79	5.09	7.27
Case 20 (APHMAXSSL180 [no B_c])	3.13	2.69	0.43	6.26	1.00	6.94
19−20 average (APH [no B_c])	1.79	2.41	0.32	4.52	1.52	7.04
Case 21 (PERMINSSL180 [no B_c])	0.71	2.24	0.23	3.19	3.47	7.29
Case 22 (PERMAXSSL180 [no B_c])	5.41	2.51	0.56	8.48	0.57	6.58
21−22 average (PER [no B_c])	3.06	2.38	0.40	5.84	0.90	6.78

select the integral spherical surface to be 6 R_M. The results are quite interesting, and several conclusions can be made.

3.1. Effects of Crustal Field Orientation

First, the crustal magnetic field has a shielding effect to protect Mars from the solar wind interaction and is therefore able to reduce the ion escape rates. For example, comparison of cases in the AEQUMIN conditions (cases 7−9) shows that case 8 (SSL = 180°W, crustal field, B_c, mainly faces the Sun) has the smallest net ion escape rate (O^+, O_2^+, and CO_2^+) and case 7 (SSL = 0°W, B_c mainly faces the tail region) has the largest net ion escape rate among these three cases. Interestingly, the same conclusion is not valid for aphelion and perihelion conditions due to the axial tilt, inhomogenous distribution of the crustal field, and possibly the 3-D atmosphere profiles (e.g., the effect of surface albedo and thermal inertia in M-GITM). For aphelion conditions, even when SSL = 180 (cases 2 and 5), the crustal magnetic field is mainly concentrated in the southern
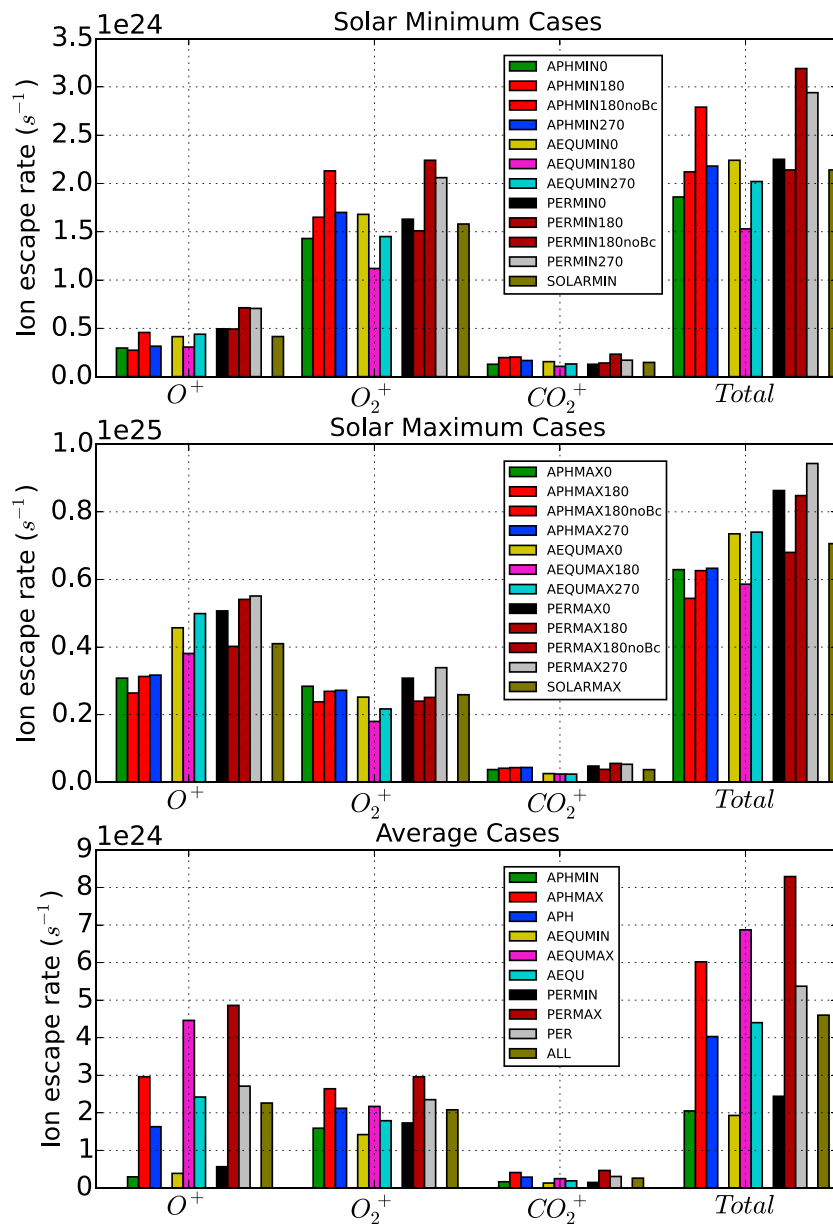
Figure 4. The histograms of ion escape rates (in s^{-1}). (top) Cases with solar minimum conditions, (middle) cases with solar maximum conditions, and (bottom) average cases. Noted that the ion escape rate scales in these three plots are different.

hemisphere polar region in the MSO coordinate system (as indicated by Figure 2). Therefore, the crustal field does not play a significant role in the solar wind-Mars interaction like in the equinox cases. For perihelion conditions, when SSL = 180 (cases 14 and 17), the crustal magnetic field is mainly concentrated in the dayside equatorial region (almost exactly facing the Sun). The shielding effect of the crustal field under this circumstance is stronger than those in the equinox cases.

Contrary to our initial expectation, the smallest net escape rate is associated with the AEQUMIN conditions when the crustal magnetic field faces the Sun (case 8, 1.53 ×10^{24} s^{-1}) instead of the APHMIN conditions with the same crustal field orientation (case 2, 2.12 ×10^{24} s^{-1}). This behavior indicates that considering only the heliocentric distance or the associated chemical reaction rates is not sufficient to determine the ion escape rates due to the influence of the crustal magnetic field. According to our simulation, case 18 (PER-MAX, SSL = 270) has the largest net ion escape rate, 9.43 ×10^{24} s^{-1}. Although the existence of the axial tilt and the potential influence of the 3-D atmosphere can break the simple conclusion we draw for the equinox

conditions, overall the crustal field shows a strong shielding effect to prevent the ion loss from the solar wind-Mars interaction. It is interesting to point out that both hybrid models [e.g., *Brecht and Ledvina*, 2014a] and other MF-MHD codes [e.g., *Harnett and Winglee*, 2006] also showed that the crustal field has a strong shielding effect to protect Mars from the solar wind interaction regardless of different model setups and inputs. Meanwhile, *Riousset et al.* [2014] pointed out that the ionospheric outflows are likely to be prevented when the surface and lower atmospheres are shielded by closed field lines due to the presence of magnetic loops and arcades. Such shielding ultimately reduces the fluxes of ions from the dynamo region to the upper ionosphere and thus reducing the ion escape rate. Furthermore, *Lundin et al.* [2011] studied how the ionospheric O^+ outflow and escape are related to the crustal magnetic field regions by analyzing the ASPERA-3 data from MEX. They found that a large fraction of the energized O^+ ions remain magnetically trapped and are recycled within the minimagnetospheres generated by the small-scale planetary crustal field regions at Mars. When the crustal field faces the Sun, it has an effect to deviate the dayside ion flow and thus reducing the tailward transport and escape of ionospheric plasma.

3.2. Effects of Seasonal Variations

Second, by averaging over different crustal field orientations and solar cycle conditions, we found that aphelion conditions (APH) are associated with a net ion escape rate of 4.03×10^{24} s^{-1}, autumnal equinox conditions (AEQU) are associated with a net ion escape rate of 4.40×10^{24} s^{-1}, and perihelion conditions (PER) yield an increased net ion escape rate up to 5.37×10^{24} s^{-1}. As expected, perihelion has the largest net ion escape rate, and aphelion has the smallest total ion loss rate. According to the values mentioned above, the seasonal variations may cause a factor of $\sim$1.33 variation in the ion loss rate.

Although we try to eliminate the effect of crustal field when estimating the ion escape affected by seasonal variations alone, the crustal field still has a potential effect on the results due to the axial tilt. In other words, the seasonal variations and crustal magnetic field orientations are closely connected with each other and may not be simply decoupled by averaging over different B_c orientations and solar cycles. With different crustal field orientations but the same solar cycle and seasonal conditions, we calculated the ratio of maximum net ion loss to minimum ion loss for APHMIN (2.18/1.86$\sim$1.17), APHMAX (6.33/5.44$\sim$1.16), and the average of APHMIN and APHMAX, APH ($\sim$1.17); AEQUMIN (2.24/1.53$\sim$1.46), AEQUMAX (7.40/5.86$\sim$1.26), and AEQU ($\sim$1.36); PERMIN (2.94/2.14$\sim$1.37), PERMAX (9.43/6.80$\sim$1.39), and PER ($\sim$1.38). Based on the results, we could easily prove that the shielding effect of crustal field are significantly correlated with season. Figure 4 may help to illustrate this conclusion in a more intuitive way. The crustal field has a more significant shielding effect for perihelion conditions than for the aphelion conditions due to the axial tilt.

In order to investigate the seasonal control of the ion loss more accurately, we calculated four more cases without the crustal magnetic field: APHMIN, APHMAX, PERMIN, and PERMAX, in which all SSL = 180°W. Surprisingly, we obtained a factor of $\sim$1.29 variation in the ion escape due to different seasons, which is only slightly smaller (within 5%) than the previous estimate $\sim$1.33, based on the average of results obtained with three crustal field orientations. Therefore, it may be appropriate to estimate the seasonal control of the ion loss by averaging over different crustal field orientations, but further investigations with more crustal field orientations or a real-time case are needed to verify this argument. Compared with the corresponding cases with crustal magnetic fields, all the ion escape rates increase (also see Figure 4) when crustal field is turned off, consistent with the first conclusion drawn above. On the other hand, the ion escape rate of case 18 is generally higher than that of case 22, indicating that the crustal field may also help ions to escape from the Martian upper atmosphere under certain circumstances, e.g., magnetic reconnection. The results may also be caused by the different M-GITM atmospheric profiles (with different subsolar longitudes) used in these two cases. Currently, surface albedo and thermal inertia are the only two parameters implemented into M-GITM that can affect atmospheric profiles during Mars' rotation [*Bougher et al.*, 2015]. In other words, if one turns off these two parameters, all the atmospheric profiles are identical regardless of the subsolar longitude. Although these two parameters may affect the upper atmosphere profile to some extent, they are more important for the lower atmospheric structure via the radiative transfer process. At present, M-GITM does not include surface topography.

3.3. Effects of Solar Cycle Conditions

Third, by averaging over different crustal field orientations and seasonal variations, we obtained that the net ion escape rate for solar maximum conditions (SOLARMAX, 7.06×10^{24} s^{-1}) is about 3.3 times higher than that of solar minimum conditions (SOLARMIN, 2.14×10^{24} s^{-1}). In other words, different solar cycles can affect the
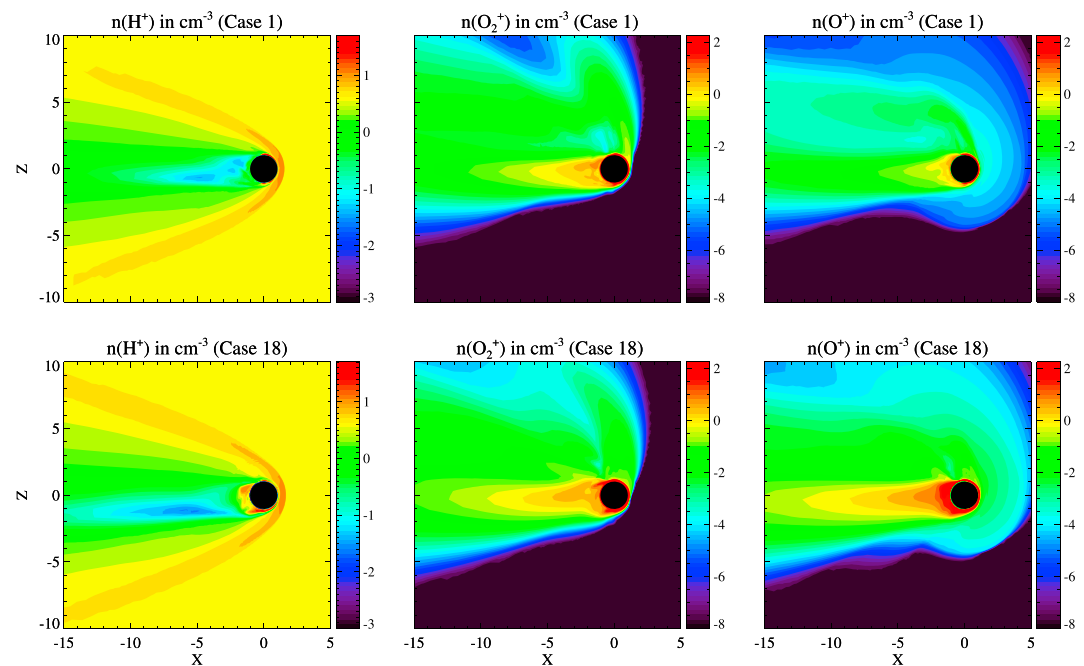
Figure 5. The calculated ion number densities in cm^{-3} in the x-z plane for H$^+$, O$_2^+$, and O$^+$ in a logarithmic scale. (top row) Case 1 is shown, and (bottom row) case 18 is shown. Noted that the logarithmic scales in different plots are different. The direction of the solar wind is parallel to the x axis and in the −x direction.

ion escape rate by a factor of ~3.3 based on our simulations. Our calculated total ion escape rate for SOLARMIN conditions is ~2 ×10^{24} s^{-1}, in reasonable agreement with the MEX data as shown in Figure 4 in *Lundin et al.* [2013]. For SOLARMAX conditions, the calculated result is 7.06 ×10^{24} s^{-1}, which is also reasonably consistent with the ion escape rate estimate from MEX data, ~1 ×10^{25} s^{-1} [*Lundin et al.*, 2013]. The increasing trend of the ion escape rate with solar activity is somewhat different from that reported by *Lundin et al.* [2013] (a factor of ~10). One possible explanation is that we did not include the neutral wind in our simulations, which can greatly affect the ion loss [*Brecht and Ledvina*, 2014b]. On the other hand, the recent paper published by *Ramstad et al.* [2015] showed that the solar wind density and velocity can greatly affect the ratio of escape rate between low and high solar EUV conditions. They adopted more than 7 years of ion flux measurements in the energy range 10 eV to 15 keV from ASPERA-3/IMA instrument on board MEX. As shown in their Figure 5, it is clear that based on our simulation parameters (solar wind velocity 400 km and solar wind density 4 cm^{-3}), the escape rate ratio is less than a factor of 10.

A careful analysis of individual mass spectra in *Lundin et al.* [2009] shows that the CO$_2^+$ contribution to the low-energy (<300 eV) heavy ion outflow is ≤10%. On average, our CO$_2^+$ ion contribution to the total ion escape (O$^+$, O$_2^+$, and CO$_2^+$) is about 6.85% for SOLARMIN conditions and 5.30% for SOLARMAX conditions; both these values and the ratio from ALL conditions (as shown in Table 2, ~5.66%) are consistent with the observations (<10%). *Nilsson et al.* [2011] pointed out that the average flux ratio of the molecular species (O$_2^+$ and CO$_2^+$) to O$^+$ ions is 0.9 ± 0.1 based on the statistics of MEX data from May 2007 to May 2011 for ion energies below 50 eV. Our escape rate ratio of molecular (O$_2^+$ and CO$_2^+$) to O$^+$ ions varies case by case as shown in Table 2. Since the estimate by *Nilsson et al.* [2011] is based upon a 4 year average, the calculated ratio should be independent of seasonal variations given the fact that one Martian year is approximately equal to two Earth's years. Based on our calculations, this ratio is ~4.16 for SOLARMIN conditions and 0.72 for SOLARMAX conditions. The average over solar cycles leads to a ratio of 1.04 (ALL conditions as shown in Table 2), in good agreement with the MEX data. The MEX data used in previous studies [*Nilsson et al.*, 2011] was collected only from low solar activity to moderate level, but our result is based on the average over two solar cycle conditions. The other important factor that can lead to a difference is that their estimate of the flux ratio was based on ion energies below 50 eV, while our calculations include ions from all energy ranges. The low-energy limit in their calculation underestimates the high-energy escape ions. It is noteworthy that although M-GITM and M-AMPS provide the MF-MHD code with more realistic 3-D cold and hot neutral atmosphere profiles
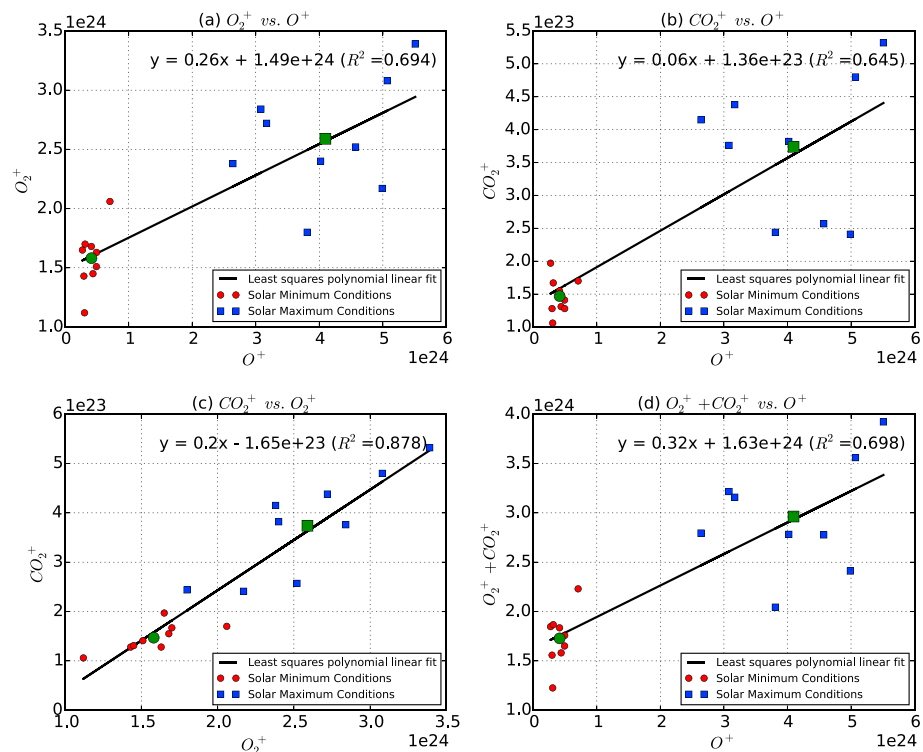
Figure 6. Least squares polynomial linear fit of the simulation results based on cases 1–18. The calculated ion escape rates associated with solar minimum and solar maximum conditions are indicated by the red circle and blue square markers, respectively. The corresponding mean values are highlighted by the green markers with the same shape.

(Figures 2 and 3), currently there are few accurate measurements of the (thermal and suprathermal) oxygen profiles in the Mars atmosphere [*Bougher et al.*, 2014]. This uncertainty affects the calculated ion escape rates. Therefore, the neutral atmosphere profiles to be returned by the MAVEN mission will significantly reduce the uncertainty in calculated escape rates resulting from the lack of direct information regarding the cold and hot oxygen abundances.

Figure 5 shows a comparison of H^+, O_2^+, and O^+ ion escape plumes in the *x-z* plane of the MSO coordinate system for two extreme cases: APHMIN (case 1) and PERMAX (case 18). The main feature of the MF-MHD model is the asymmetric escape plume for heavy ion (O^+, O_2^+) species. The lack of significant escape plume for H^+ ions is because of its small mass (and thus small gyroradius) and the fact that the solar wind and ionospheric protons are combined in the model [*Najib et al.*, 2011]. The plume provides a channel for ions to escape which cannot be reproduced by the multispecies MHD model [*Ma et al.*, 2004; *Ma and Nagy*, 2007]. The asymmetry is primarily caused by different Lorentz forces acting on each ion species [*Najib et al.*, 2011; *Dong et al.*, 2014]. From the particle simulation point of view, the asymmetry can also be explained by the induced electric field [*Fang et al.*, 2010; *Curry et al.*, 2013, 2014]. From Figure 5, it is not difficult to distinguish the aphelion case from the perihelion case according to the different strengths of the ion escape plume, primarily caused by different solar radiation. Figure 5 (top row) is associated with aphelion conditions which has a weaker ion escape plume than Figure 5 (bottom row) for perihelion conditions, especially when focusing on the hot oxygen corona region of the contour plot. The contour plots shown in Figure 5 are also consistent with the hot oxygen profiles shown in Figure 3 and the ion escape rates shown in Table 2.

3.4. Effects of Mass Differentiation

Last but not least, all the ion escape rates show a positive linear correlation with each other (Figure 6). The cold heavy ionospheric molecular ion escape fraction [(O_2^+ and/or CO_2^+)/Total] is inversely proportional to the atomic ion escape fraction [O^+/Total], whereas O_2^+ and CO_2^+ ion escape fractions show a positive linear correlation (Figure 7). The escape fraction is defined as the escape rate ratio between an individual or sum of several ion species to total ions. The positive linear correlation in Figure 6 is mainly caused by the fact that an increase in solar irradiance leads to a higher amount of ionized gas via photoionization. Although the
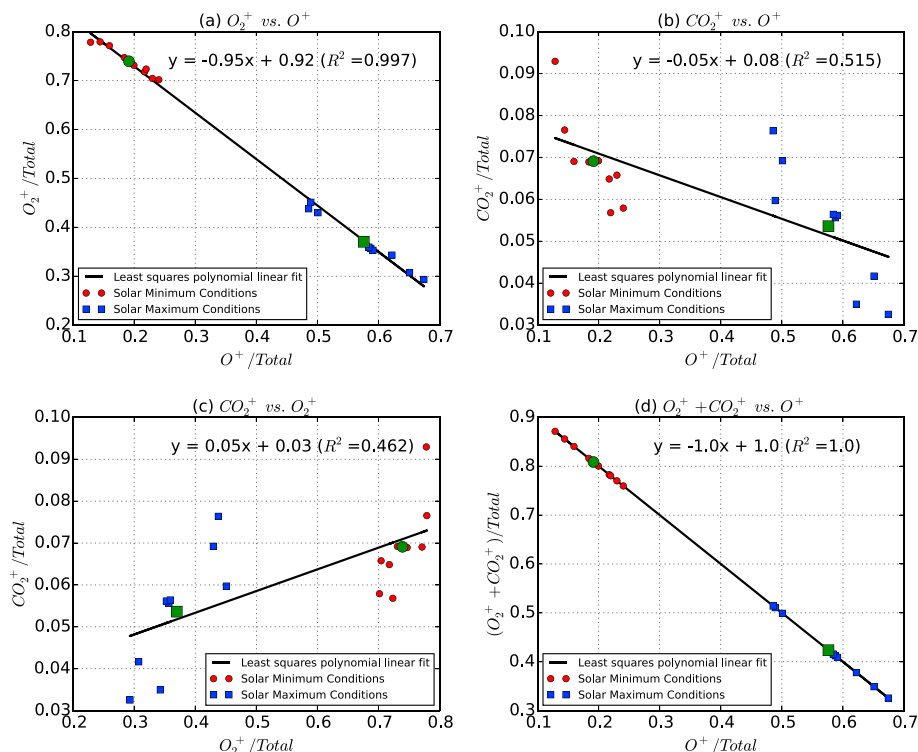
Figure 7. Least squares polynomial linear fit of the simulation results based on cases 1–18. The calculated ion escape rate fractions (with respect to the net ion loss) associated with solar minimum and solar maximum conditions are indicated by the red circle and blue square markers, respectively. The corresponding mean values are highlighted by the green markers with the same shape. Although the perfect linear anticorrelation in Figure 7d is mathematically to be expected, all the linear correlations indicated in Figure 7 can also be physically interpreted.

perfect linear anticorrelation in Figure 7d is mathematically to be expected, all the linear correlations indicated in Figure 7 can also be physically interpreted. As we mentioned above, Mars has a solar cycle-dependent hot atomic oxygen corona (see Figure 3), which is ionized by the solar radiation and the solar wind electrons via photoionization and electron impact ionization, respectively. The ionized O^+ can be picked up by the solar wind and escape from the Martian upper atmosphere. The mass loading process reduces the solar wind speed and the dynamic pressure, and thus, the solar wind has a reduced opportunity to penetrate deeply into the Martian ionosphere mainly due to the momentum conservation. As a result, the cold heavy ionospheric molecular ions (O_2^+ and CO_2^+) are relatively less affected by the solar wind, and the associated ion escape rate fraction [($O_2^+ + CO_2^+$)/Total] is decreased. Besides, the ionized hot oxygen corona behaves approximately as a perfect conductor and therefore prevents the electric and magnetic fields from penetrating into the Martian ionosphere to a certain degree. Both the mass loading and electromagnetic shielding contribute to the inverse correlation between the cold heavy ionospheric molecular ion escape fraction [(O_2^+ and/or CO_2^+)/Total] and the atomic ion escape fraction [O^+/Total]. Meanwhile, O_2^+ and CO_2^+ ion escape fractions (ionospheric ion outflow) show a positive linear correlation (r value = 0.68) because both species are originated from the cold Martian ionosphere and should follow the same escape path. In order to avoid any artificial factor resulting from both the small data sets and missing the solar moderate cases, we decided to adopt the linear regression rather than a cubic polynomial regression fit to increase the correlation coefficient (r value). In the future work, we plan to add the data sets from the solar moderate cases for the linear regression, most of which should lie in the middle of Figures 6 and 7, and thus may help increase the r value.

In Figures 6 and 7, the calculated ion escape rates and the ion escape rate fractions (with respect to the total ion loss) associated with solar minimum and solar maximum conditions are indicated by the red circle and blue square markers, respectively. The corresponding mean values are highlighted by the green markers with the same shape in both figures. The least squares polynomial linear fit of the simulation results based on cases 1–18 (two average green points are not included) is shown in each figure as well. Correlations among different ion escape rates and the corresponding correlations among their fractions for different solar cycle conditions

Table 3. Slope and Intercept of the Regression Line Shown in Figure 7, Correlation Coefficient (*r* Value), Coefficient of Determination (*r* Squared, R^2), Two-Sided *p* Value for a Hypothesis Test Whose Null Hypothesis Is That the Slope Is Zero, Standard Error of the Estimate (stderr)

	Slope	Intercept	*r* Value	R^2	*p* Value	stderr
O_2^+ versus O^+	0.264	1.49×10^{24}	0.833	0.694	1.776×10^{-5}	0.0438
CO_2^+ versus O^+	0.0553	1.357×10^{23}	0.803	0.645	5.949×10^{-5}	0.0103
CO_2^+ versus O_2^+	0.204	-1.647×10^{23}	0.937	0.878	9.95×10^{-9}	0.019
$O_2^+ + CO_2^+$ versus O^+	0.319	1.626×10^{24}	0.835	0.698	1.592×10^{-5}	0.0525
O_2^+ versus O^+ (fraction)	−0.948	0.919	−0.999	0.997	7.791×10^{-22}	0.0126
CO_2^+ versus O^+ (fraction)	−0.052	0.081	−0.718	0.515	8.015×10^{-4}	0.0126
CO_2^+ versus O_2^+ (fraction)	0.052	0.033	0.680	0.462	1.922×10^{-3}	0.014
$O_2^+ + CO_2^+$ versus O^+ (fraction)	−1.0	1.0	−1.0	1.0	5.027×10^{-159}	0.0

help us to understand the physics behind the regression lines. For example, during the period of high solar activity, Mars has a more extensive hot oxygen corona (see Figure 3), so the O^+ ion escape fraction is relatively large in Figure 7 (mainly distributed in the lower right corner when O^+/Total is the horizontal axis) while the cold heavy ionospheric molecular ion escape fraction is relatively small. The associated statistical details, e.g., slope and intercept of the regression line, correlation coefficient (*r* value), coefficient of determination (*r* squared, R^2), two-sided *p* value and standard error of the estimate (stderr) are shown in Table 3.

The *r* value is a measure of the linear correlation (dependence) between two variables *X* and *Y*, giving a value between +1 and −1, where 1 is total positive correlation, 0 is no correlation, and −1 is total negative correlation. It is defined as the (sample) covariance of the variables divided by the product of their (sample) standard deviations. The coefficient of determination, denoted R^2 or r^2, is a number that indicates how well data fit a statistical model. The Two-sided *p* value indicates the probability of the correlation occurring by random chance. The standard error of the estimate (stderr) represents the average distance that the observed values fall from the regression line. Conveniently, it tells you how wrong the regression model is on average using the units of the response variable. Smaller values are better because it indicates that the observations are closer to the fit line. The linear correlation in Figures 6 and 7 is very useful when one does not have all the ion escape information and/or the spacecraft instrument mass resolution is not high enough to distinguish ion species, e.g., O^+ and O_2^+. Knowing the total ion and O^+ ion escape rates, the cold heavy ionospheric molecular ion escape rate can simply be calculated based on the linear fits shown in Figure 7d. If one needs to distinguish between O_2^+ and CO_2^+, the linear fit in the plot of CO_2^+ versus O_2^+ (Figure 6c) can be used.

In addition to the comparison with the available MEX data, we also list our predictions here for the data to be returned by the MAVEN mission. Once the MAVEN data sets become available, we will conduct a detailed comparison between the three model results and MAVEN observational data. Such comparisons are essential to provide new insights by coupling the three codes and to identify possible missing physics for future incorporation into the models. On the other hand, these 3-D simulations can provide global context for individual measurements; i.e. for example, predictions of the time history and certain physical problems of interest, based on the limited spacecraft data, are possible. It will be instructive to run a real-time case in the near future with the variable solar wind parameters (density and velocity) from the solar wind ion analyzer (SWIA) and the IMF from the magnetometer (MAG) instruments. Finally, investigators need to be careful when they calculate the controlling factors regulating the seasonal variations of the solar wind interaction. The coexistence of effects due to both crustal field location and the planetary axial tilt may influence the estimate to a certain degree.

4. Conclusions

In summary, we studied the solar wind interaction with the Martian upper atmosphere by using one-way coupling of three comprehensive 3-D models; i.e., both the M-GITM thermosphere-ionosphere outputs and the M-AMPS exosphere hot atomic oxygen are used as inputs for the MF-MHD model. The effects of crustal field orientation, solar cycle, and seasonal variations on the Martian upper atmosphere ion escape are investigated in detail by comparing 22 cases. Different solar cycles can affect the ion loss by a factor of ~3.3, while different seasons can vary the ion loss by a factor of ~1.3. The coexistence of crustal field and axial tilt lead to a quite

intricate solar wind-Mars interaction. There is no simple conclusion that a certain crustal magnetic field orientation can lead to the smallest ion escape rate as found in previous studies [e.g., *Ma and Nagy*, 2007]. Instead, in this study, we found that the smallest ion escape rate also depends on the seasonal variations due to the axial tilt and the 3-D atmospheric structure. Overall, it is clear that the crustal magnetic field has a shielding effect to protect Mars from the solar wind interaction, and this effect is the strongest for perihelion conditions with the crustal field facing the Sun. Furthermore, the cold heavy ionospheric molecular ion escape fraction [(O_2^+ and/or CO_2^+)/Total] is inversely proportional to the atomic ion escape fraction [O^+/Total]. On the other hand, O_2^+ and CO_2^+ ion escape fractions (ionospheric ion outflow) show a positive linear correlation.

Contrary to our initial expectation, the smallest total ion escape rate is associated with the autumnal equinox solar minimum (AEQUMIN) case instead of the aphelion solar minimum (APHMIN) case, again due to the effect of coexisting crustal field and axial tilt plus the 3-D atmosphere. Based on averages over different solar cycles and various crustal field orientations, perihelion conditions yield the highest total ion escape rate and aphelion conditions yield the lowest total ion escape rate, which is well within our expectations. The calculated ion escape rates are in reasonable agreement with the recent observational data from MEX. For solar minimum conditions, the total ion (O^+, O_2^+, and CO_2^+) escape rate is around 2.0×10^{24} s^{-1} and for solar maximum conditions, the net ion loss is 7.06×10^{24} s^{-1}. By averaging our 18 MHD model cases, we obtained CO_2^+/Total ($\sim$5.66%) and ($CO_2^+ + O_2^+$)/O^+ ($\sim$1.04), which are consistent with the statistical results from 4 year MEX observational data.

This work aims to build a model library for the MAVEN mission, which has the potential to provide improved predictions of ion escape rates for comparison to future data to be returned by the MAVEN mission (2014–2016) and thereby improve our understanding of present escape processes. Estimates of ion escape rates over Mars history must start from properly validated models that can be extrapolated into the past. This work will enhance the science return from the MAVEN mission.

References

Acuña, M. H., et al. (1999), Global distribution of crustal magnetization discovered by the Mars global surveyor MAG/ER experiment, *Science*, *284*, 790–793.

Arkani-Hamed, J. (2001), A 50-degree spherical harmonic model of the magnetic field of Mars, *J. Geophys. Res.*, *106*, 23,197–23,208.

Barabash, S., A. Fedorov, R. Lundin, and J. A. Sauvaud (2007), Martian atmospheric erosion rates., *Science*, *315*, 501–503.

Bird, G. A. (1994), *Molecular Gas Dynamics and the Direct Simulation of Gas Flows*, 2nd ed., Clarendon Press, Oxford.

Bougher, S. W., S. Engel, R. G. Roble, and B. Foster (2000), Comparative terrestrial planet thermospheres: 3. Solar cycle variation of global structure and winds at solstices, *J. Geophys. Res.*, *105*, 17,669–17,692.

Bougher, S. W., J. M. Bell, J. R. Murphy, M. A. Lopez-Valverde, and P. G. Withers (2006), Polar warming in the Mars thermosphere: Seasonal variations owing to changing insolation and dust distributions, *Geophys. Res. Lett.*, *33*, L02203, doi:10.1029/2005GL024059.

Bougher, S. W., P.-L. Blelly, M. R. Combi, J. L. Fox, I. Mueller-Wodarg, A. Ridley, and R. G. Roble (2008), Neutral upper atmosphere and ionosphere modeling, *Space Sci. Rev.*, *139*, 107–141.

Bougher, S. W., T. E. Cravens, J. Grebowsky, and J. Luhmann (2014), The aeronomy of Mars: Characterization by MAVEN of the upper atmosphere reservoir that regulates volatile escape, *Space Sci. Rev.*, doi:10.1007/s11214-014-0053-7, in press.

Bougher, S. W., D. J. Pawlowski, J. M. Bell, S. Nelli, T. McDunn, J. R. Murphy, M. Chizek, and A. Ridley (2015), Mars Global Ionosphere-Thermosphere Model (M-GITM): Solar cycle, seasonal, and diurnal variations of the Mars upper atmosphere, *J. Geophys. Res. Planets*, *120*, 311–342, doi:10.1002/2014JE004715.

Brain, D., et al. (2010), A comparison of global models for the solar wind interaction with Mars, *Icarus*, *206*, 139–151.

Brain, D., et al. (2012), Comparison of global models for the escape of Martian atmospheric plasma, AGU Fall Meeting Abstracts, P13C-1969.

Brecht, S. H., and S. A. Ledvina (2014a), The role of the Martian crustal magnetic fields in controlling ionospheric loss, *Geophys. Res. Lett.*, *41*, 5340–5346, doi:10.1002/2014GL060841.

Brecht, S. H., and S. A. Ledvina (2014b), Hybrid particle code simulations of Mars: The role of assorted processes in ionospheric escape, AGU Fall Meeting Abstracts, P54A-06.

Cravens, T. E., J. U. Kozyra, A. F. Nagy, T. I. Gombosi, and M. Kurtz (1987), Electron impact ionization in the vicinity of comets, *J. Geophys. Res.*, *92*, 7341–7353.

Curry, S. M., M. W. Liemohn, X.-H. Fang, Y.-J. Ma, and J. Espley (2013), The influence of production mechanisms on pick-up ion loss at Mars, *J. Geophys. Res. Space Physics*, *118*, 554–569, doi:10.1029/2012JA017665.

Curry, S. M., M. W. Liemohn, X.-H. Fang, Y.-J. Ma, J. Slavin, J. Espley, S. Bougher, and C. F. Dong (2014), Test particle comparison of heavy atomic and molecular ion distributions at Mars, *J. Geophys. Res. Space Physics*, *119*, 2328–2344, doi:10.1002/2013JA019221.

Curry, S. M., J. G. Luhmann, Y. Ma, M. W. Liemohn, C. Dong, and T. Hara (2015), Comparative pick-up ion distributions at Mars and Venus: Consequences for atmospheric deposition and escape, *Planet. Space Sci.*, *115*, 35–47, doi:10.1016/j.pss.2015.03.026.

de Pater, I., and J. J. Lissauer (2010), *Planetary Sciences*, 2nd ed., pp. 5–6, Cambridge Univ. Press, New York.

Deng, Y., A. D. Richmond, A. J. Ridley, and H.-L. Liu (2008), Assessment of the non-hydrostatic effect on the upper atmosphere using a general circulation model (GCM), *Geophys. Res. Lett.*, *35*, L01104, doi:10.1029/2007GL032182.

Dong, C., S. W. Bougher, Y. Ma, G. Toth, A. F. Nagy, and D. Najib (2014), Solar wind interaction with Mars upper atmosphere: Results from the one-way coupling between the multifluid MHD model and the MTGCM model, *Geophys. Res. Lett.*, *41*, 2708–2715, doi:10.1002/2014GL059515.

Fang, X., M. W. Liemohn, A. F. Nagy, J. G. Luhmann, and Y. J. Ma (2010), On the effect of the Martian crustal magnetic field on atmospheric erosion, *Icarus*, *206*, 130–138.

Feldman, P. D., et al. (2011), Rosetta-Alice observations of exospheric hydrogen and oxygen on Mars, *Icarus*, *214*, 394–399.

Glocer, A., G. Tóth, Y. J. Ma, T. I. Gombosi, J. C. Zhang, and L. M. Kistler (2009), Multifluid Block-Adaptive-Tree Solar wind Roe-type Upwind Scheme: Magnetospheric composition and dynamics during geomagnetic storms—Initial results, *J. Geophys. Res.*, *114*, A12203, doi:10.1029/2009JA014418.

Haberle, R. M., M. M. Joshi, J. R. Murphy, J. R. Barnes, J. T. Schofield, G. Wilson, M. Lopez-Valverde, J. L. Hollingsworth, A. F. C. Bridger, and J. Schaeffer (1999), General circulation model simulations of the Mars Pathfinder atmospheric structure investigation/meteorology data, *J. Geophys. Res.*, *104*, 8957–8974.

Harnett, E. M., and R. M. Winglee (2006), Three-dimensional multifluid simulations of ionospheric loss at Mars from nominal solar wind conditions to magnetic cloud events, *J. Geophys. Res.*, *111*, A09213, doi:10.1029/2006JA011724.

Johnson, R. E., and J. G. Luhmann (1998), Sputter contribution to the atmospheric corona on Mars, *J. Geophys. Res.*, *103*, 3649–3653.

Kim, J., A. F. Nagy, J. L. Fox, and T. E. Cravens (1998), Solar cycle variability of hot oxygen atoms at Mars, *J. Geophys. Res.*, *103*(A12), 29,339–29,342, doi:10.1029/98JA02727.

Lee, Y., M. R. Combi, V. Tenishev, and S. W. Bougher (2013), Hot oxygen corona in Mars' upper thermosphere and exosphere: A comparison of results using the MGITM and MTGCM, AGU Fall Meeting Abstracts, P21A-1703.

Lee, Y., M. R. Combi, V. Tenishev, and S. W. Bougher (2014a), Hot carbon corona in Mars' upper thermosphere and exosphere: 1. Mechanisms and structure of the hot corona for low solar activity at equinox, *J. Geophys. Res. Planets*, *119*, 905–924, doi:10.1002/2013JE004552.

Lee, Y., M. R. Combi, V. Tenishev, and S. W. Bougher (2014b), Hot carbon corona in Mars' upper thermosphere and exosphere: 2. Solar cycle and seasonal variability, *J. Geophys. Res. Planets*, *119*, 2487–2509, doi:10.1002/2014JE004669.

Lundin, R., S. Barabash, M. Holmström, H. Nilsson, M. Yamauchi, M. Fraenz, and E. M. Dubinin (2008), A comet-like escape of ionospheric plasma from Mars, *Geophys. Res. Lett.*, *35*, L18203, doi:10.1029/2008GL034811.

Lundin, R., S. Barabash, M. Holmström, H. Nilsson, M. Yamauchi, E. M. Dubinin, and M. Fraenz (2009), Atmospheric origin of cold ion escape from Mars, *Geophys. Res. Lett.*, *36*, L17202, doi:10.1029/2009GL039341.

Lundin, R., S. Barabash, M. Yamauchi, H. Nilsson, and D. Brain (2011), On the relation between plasma escape and the Martian crustal magnetic field, *Geophys. Res. Lett.*, *38*, L02102, doi:10.1029/2010GL046019.

Lundin, R., S. Barabash, M. Holmström, H. Nilsson, Y. Futaana, R. Ramstad, M. Yamauchi, E. M. Dubinin, and M. Fraenz (2013), Solar cycle effects on the ion escape from Mars, *Geophys. Res. Lett.*, *40*, 6028–6032, doi:10.1002/2013GL058154.

Ma, Y. J., A. F. Nagy, I. V. Sokolov, and K. C. Hansen (2004), Three-dimensional, multispecies, high spatial resolution MHD studies of the solar wind interaction with Mars, *J. Geophys. Res.*, *109*, A07211, doi:10.1029/2003JA010367.

Ma, Y. J., and A. F. Nagy (2007), Ion escape fluxes from Mars, *Geophys. Res. Lett.*, *34*, L08201, doi:10.1029/2006GL029208.

Ma, Y. J., X. Fang, C. T. Russell, A. F. Nagy, G. Toth, J. G. Luhmann, D. A. Brain, and C. Dong (2014), Effects of crustal field rotation on the solar wind plasma interaction with Mars, *Geophys. Res. Lett.*, *41*, 6563–6569, doi:10.1002/2014GL060785.

Modolo, R., G. M. Chanteur, and E. Dubinin (2012), Dynamic Martian magnetosphere: Transient twist induced by a rotation of the IMF, *Geophys. Res. Lett.*, *39*, L01106, doi:10.1029/2011GL049895.

Najib, D., A. F. Nagy, G. Tóth, and Y. J. Ma (2011), Three-dimensional, multifluid, high spatial resolution MHD model studies of the solar wind interaction with Mars, *J. Geophys. Res.*, *116*, A05204, doi:10.1029/2010JA016272.

Nilsson, H., N. J. Edberg, G. Stenberg, S. Barabash, M. Holmström, Y. Futaana, R. Lundin, and A. Fedorov (2011), Heavy ion escape from Mars, influence from solar wind conditions and crustal magnetic fields, *Icarus*, *215*, 475–484.

Powell, K. G., P. L. Roe, T. J. Linde, T. I. Gombosi, and D. L. De Zeeuw (1999), A solution-adaptive upwind scheme for ideal magnetohydrodynamics, *J. Comput. Phys.*, *154*, 284–309.

Ramstad, R., S. Barabash, Y. Futaana, H. Nilsson, X.-D. Wang, and M. Holmström (2015), The Martian atmospheric ion escape rate dependence on solar wind and solar EUV conditions: 1. Seven years of Mars Express observations, *J. Geophys. Res. Planets*, *120*, 1298–1309, doi:10.1002/2015JE004816.

Ridley, A., Y. Deng, and G. Toth (2006), The global ionosphere-thermosphere model, *J. Atmos. Sol. Terr. Phys.*, *68*, 839–864.

Riousset, J. A., C. S. Paty, R. J. Lillis, M. O. Fillingim, S. L. England, P. G. Withers, and J. P. M. Hale (2013), Three-dimensional multifluid modeling of atmospheric electrodynamics in Mars' dynamo region, *J. Geophys. Res. Space Physics*, *118*, 3647–3659, doi:10.1002/jgra.50328.

Riousset, J. A., C. S. Paty, R. J. Lillis, M. O. Fillingim, S. L. England, P. G. Withers, and J. P. M. Hale (2014), Electrodynamics of the Martian dynamo region near magnetic cusps and loops, *Geophys. Res. Lett.*, *41*, 1119–1125, doi:10.1002/2013GL059130.

Schunk, R. W., and A. F. Nagy (2009), *Ionospheres*, 2nd ed., Cambridge Univ. Press, New York.

Tenishev, V., and M. Combi (2008), A global kinetic model for cometary comae: The evolution of the coma of the Rosetta target comet Churyumov-Gerasimenko throughout the mission, *Astrophys. J.*, *685*, 659–677.

Tóth, G., et al. (2012), Adaptive numerical algorithms in space weather modeling, *J. Comput. Phys.*, *231*, 870–903.

Valeille, A., V. Tenishev, S. W. Bougher, M. R. Combi, and A. F. Nagy (2009), Three-dimensional study of Mars upper thermosphere/ionosphere and hot oxygen corona: 1. General description and results at equinox for solar low conditions, *J. Geophys. Res.*, *114*, E11005, doi:10.1029/2009JE003388.

Verigin, M., et al. (1991), Ions of planetary origin in the Martian magnetosphere (Phobos 2/TAUS experiment), *Planet. Space Sci.*, *39*, 131–137.